

Research Article

Point Load Test of Half-Cylinder Core Using the Numerical Model and Laboratory Tests: Size Suggestion and Correlation with Cylinder Core

Fengyu Ren, Huan Liu , Rongxing He, Guanghui Li, and Yang Liu 

School of Resources and Civil Engineering, Northeastern University, Shenyang 110819, China

Correspondence should be addressed to Huan Liu; gyluhuan@163.com

Received 14 August 2018; Accepted 14 October 2018; Published 4 November 2018

Guest Editor: Guang Xu

Copyright © 2018 Fengyu Ren et al. This is an open access article distributed under the Creative Commons Attribution License, which permits unrestricted use, distribution, and reproduction in any medium, provided the original work is properly cited.

The point load test (PLT) is intended as an index test for rock strength classification or estimations of other strength parameters because it is economical and simple to conduct in the laboratory and in field tests. In the literature, calculation procedures for cylinder cores, blocks, or irregular lumps can be found, but no study has researched such procedures for half-cylinder cores. This paper presents the numerical model and laboratory tests for half-cylinder and cylinder specimens. The results for half-cylinder and cylinder specimens are then presented, analysed, and discussed. A correlation of failure load between half-cylinder and cylinder specimens is established with a suitable size suggestion and correction factor. It is found that the failure load becomes stable when half-cylinder specimens have a length/diameter ratio higher than 0.9. In addition, the results show that the point load strength index (PLSI) of half-cylinder cores can be calculated using the calculation procedures for diametral testing on cylinder cores, and it is necessary to satisfy the conditions that the length/diameter ratio be higher than 0.9 and the failure load be multiplied by 0.8.

1. Introduction

The point load test (PLT) is one of the primary tests to be applied during earthwork engineering practices, such as slope stabilization works, tunnelling construction, and the design of mining support and foundation [1]. The PLT can be performed either in the field or in the laboratory since the test equipment is portable and specimens can easily be prepared for testing. For these reasons, the PLT is a more practical, time-saving, and economical method compared to the uniaxial compressive strength (UCS) test.

The PLT is based on breaking a rock specimen, which is subjected to an increasingly concentrated point load applied through a pair of conical platens [2]. Failure load, rock size, rock shape, and loading mode are used to calculate the point load strength index (PLSI or $I_{s(50)}$) [3, 4]. The PLSI is an important strength parameter index for the classification of rock strength [4–7], determination of UCS [1–4, 8–14], and estimation of strength anisotropy [4, 11, 15–17].

In general, rock specimens of PLT can be applied to cores (the diametral and axial tests), spheres, blocks, and irregular lumps. The rock specimens come in different shapes. Chau and Wei [18] and Russell and Wood [19] reported on theoretical analyses of spheres subjected to PLT. Several researchers reported the PLT of irregular lumps, but the results were very different for different rock types, and the data of tests were scattered. Wong et al. [1] studied the PLT of volcanic irregular lumps. Yin et al. [14] studied the PLT of granitic irregular lumps. Hobbs [20] studied the PLT of coal measure rocks and Portland limestone irregular lumps. Hiramatsu and Oka [21] investigated the stress state in an irregular test piece subjected to point load. Panek and Fannon [22] studied the size and shape effects in PLT of irregular lumps. Many researchers have studied the PLT of cylinder cores. Khanlari et al. [17] studied the PLT of metamorphic rocks from the cylindrical punch. Chau and Wong [23] studied the PLT (axial tests) of specimens from borehole rock cores. Palchik and Hatzor [24] studied the

point load strength of cylindrical porous chalks. Tsiambaos and Sabatakakis [25] presented laboratory testing of cylindrical sedimentary rocks under point loading. Fener et al. [26] carried out the PLT on eleven Nigde rocks. Fener and Ince [27] studied the point load strength of cylindrical specimens on granitic rocks. Consequently, diametral and axial tests of cores are generally preferred for results compared to the PLT of irregular lumps. Thus, the shapes of rock specimens can be different, but calculation procedures of PLSI are different for different shapes.

The testing and calculation procedures for PLSI have been standardized by the International Society for Rock Mechanics (ISRM) [3] and have been widely adopted. Failure load, rock size, rock shape, and loading mode affect the point load strength (Is) value; therefore, Is has been proposed to correct for a standard size of 50 mm ($Is_{(50)}$). ISRM (1985) [3] suggests $Is_{(50)}$ below:

$$Is_{(50)} = F \times Is = \frac{P}{D_e^2} \times \left(\frac{D_e}{50}\right)^{0.45}, \quad (1)$$

where F is the size correction factor ($F = (D_e/50)^{0.45}$), Is is the point load strength ($Is = P/D_e^2$) in MPa, P is the failure load in kN, and D_e is the equivalent core diameter in mm. Depending on the specimen shape and loading direction, D_e varies.

When the specimen of the core is diametrically loaded, D_e is defined as

$$D_e = D, \quad (2)$$

where D is the distance between two contact points in mm. Under this condition, D is the diameter of the cylinder cores.

When the specimen of the core is axially loaded, or the specimen consists of blocks or irregular lumps, D_e is defined as

$$D_e^2 = \frac{4WD}{\pi}, \quad (3)$$

where W is the smallest specimen width of a plane through the contact points in mm.

Although many researchers have studied the relationship between failure load and $Is_{(50)}$ for different rock types, rock sizes, rock shapes, and loading modes, no study exists on half-cylinder cores. In this study, the numerical model and laboratory tests were carried out on the cylinder and half-cylinder specimens, and the correlations between the cylinder and the half-cylinder specimens were investigated. The main objective of the research reported in this paper is to determine $Is_{(50)}$ of the half-cylinder cores.

2. Half-Cylinder Cores

In the design phase of the mining method, it was necessary to take several factors into consideration. The mechanical parameters of the rock were the basis index for evaluating the stability and caveability and determining the management method of stope ground pressure and the structural parameters of stope. Therefore, we obtained the detailed rock mechanics parameters in the mining design phase,

which were significant in making the choice in the design of mining methods. However, there was no mining excavation engineering in the mining design phase, and a large number of rock specimens could not be obtained. The Luoboling Copper-Molybdenum mine was used in the design phase, and block caving was determined initially. One major problem for the mine was determining how to get more detailed rock mechanics parameters and their distribution to guide the mining engineering design.

A total of 176 boreholes were completed at the exploration stage of the Luoboling Copper-Molybdenum mine. The cylinder core was cut into two pieces (the half-cylinder cores); one piece was analysed to determine the composition and content of the copper-molybdenum, and another piece was kept aside. Therefore, half-cylinder cores were kept (Figure 1). The purpose of this study was to determine the PLSI of rock using these half-cylinder cores.

First, 18 granodiorite specimens of the half-cylinder core were taken in the same borehole. According to the size requirements of ISRM, the loading direction of PLT was along the radial direction of the half-cylinder core specimens. The specimens after the break are shown in Figure 2. Second, according to the calculation procedures of ISRM, we removed two test values of the fracture surfaces which passed through only one loading point, and we deleted the two highest and lowest values from the 16 valid values. Then, the mean value of $Is_{(50)}$ was calculated using the 12 remaining values.

The loading direction of half-cylinder specimens was along the radial direction, and the shape was not a cylinder. Therefore, we adopted two calculation procedures for the half-cylinder cores. Method 1 (M1) was based on the calculation procedure of diametral PLT on cylinder cores, formulae (1) and (2). Method 2 (M2) was based on the calculation procedure of PLT on irregular lumps, formulae (1) and (3). Figure 3 shows results by M1 and M2. According to M1, $Is_{1(50)} = 4.526$ MPa, and the coefficient of variation (CV) (the standard deviation to the mean) was calculated as $CV_1 = 0.242$. According to M2, $Is_{2(50)} = 2.444$ MPa, $CV_2 = 0.442$. There was a big difference in $Is_{(50)}$ and CV for M1 and M2. However, CV_1 was less than CV_2 , and the measured value of W was not accurate to subjective experience and external factors. Therefore, if the relationship between the cylinder and half-cylinder cores was determined in PLT, the test process could be simplified and test efficiency could be improved.

3. Numerical Model

Point load tests in the field or laboratory are time-consuming, labourious, and lack reproducibility. In addition, because the rock specimens had multiple fractures and porosities, the variation coefficients of the test results were large. However, the numerical model ensured the consistency of mechanical properties.

The numerical simulation was carried out using the distinct element method (DEM) [28]. The dynamical equation of the DEM was established using Newton's laws of motion. The spherical particle was the basic element in the

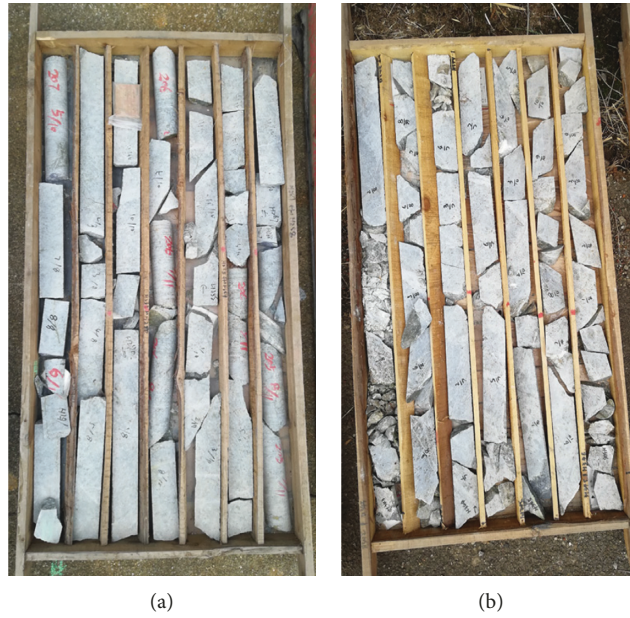


FIGURE 1: Half-cylinder cores.

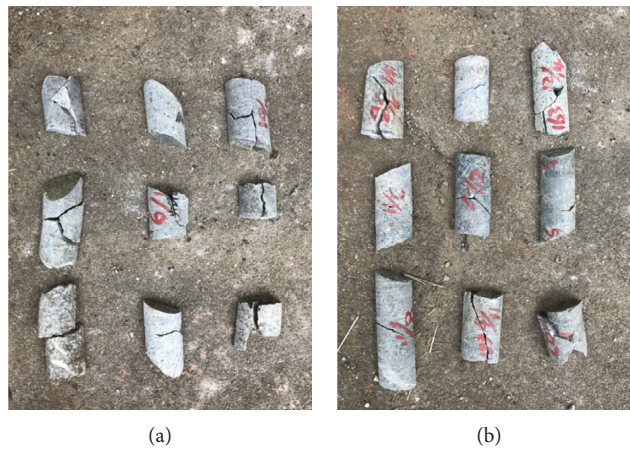


FIGURE 2: The half-cylinder cores after breaking under PLT.

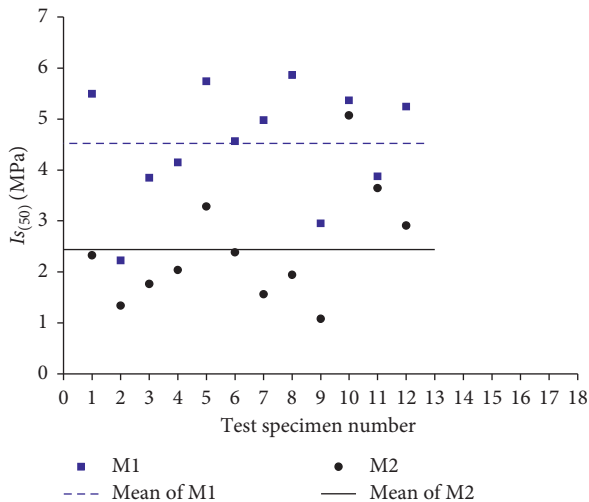


FIGURE 3: The results of $I_{s(50)}$ using various calculation procedures.

DEM. Particles interacted at pairwise contacts by means of an internal force and moment. Contact mechanics were embodied in particle-interaction laws that updated the internal forces and moments. The DEM model provided a synthetic material consisting of an assembly of rigid grains that interacted at contacts, and it included both granular and bonded materials. Moreover, it was possible to create bonded materials with half-cylinder and cylinder cores.

3.1. Contact Models. In this study, the half-cylinder and cylinder specimens of the numerical model were built through the flat-joint model (FJM) in DEM [29]. The flat-joint model could be applied to hard rock by introducing a polygonal grain structure to provide rotational restraint arising from intergranular interlock [29–31].

Each spherical particle element carries a contact force ($F^{(e)}$). The element contact forces produce a statically

equivalent force (F_c) at the centre of the interface given by [29]

$$F_c = \sum_{\forall e} F^{(e)}. \quad (4)$$

The element contact force ($F^{(e)}$) is decomposed into a normal and a shear force ($F_n^{(e)}$ and $F_s^{(e)}$) [29]:

$$F_n^{(e)} = \int_e \sigma dA = \begin{cases} 0, & \text{unbonded and } g^{(e)} \geq 0, \\ k_n g^{(e)} A^{(e)}, & \text{otherwise,} \end{cases}$$

$$F_s^{(e)} = F_s^{(e)} - k_s A^{(e)} \Delta \widehat{\delta}_s^{(e)}, \quad (5)$$

where σ is the interface normal stress, k_n is the normal stiffness, $g^{(e)}$ is the gap at the element centroid, $A^{(e)}$ is the area of each element, k_s is the shear stiffness, and $\Delta \widehat{\delta}_s^{(e)}$ is the effective portion of the relative shear-displacement increment at the element centroid.

The element normal and shear stresses ($\sigma^{(e)}$ and $\tau^{(e)}$) are given by [29]

$$\sigma^{(e)} = \frac{F_n^{(e)}}{A^{(e)}},$$

$$\tau^{(e)} = \frac{\|F_s^{(e)}\|}{A^{(e)}}. \quad (6)$$

The shear strength $\tau_c^{(e)}$ follows the Coulomb criterion with a tension cutoff [29]:

$$\tau_c^{(e)} = c - \sigma^{(e)} \tan \phi, \quad (7)$$

where c is the bond cohesion and ϕ is the friction angle.

If the element was bonded and the tensile-strength limit (σ_c) was exceeded ($\sigma^{(e)} > \sigma_c$), then the bond broke owing to tension, and a tension fracture was generated. If the shear-strength limit ($\tau_c^{(e)}$) was exceeded ($|\tau^{(e)}| > \tau_c^{(e)}$), then the bond broke in shear, and a shear fracture was generated.

3.2. Parameters of the Numerical Model. There is no mining excavation engineering in the Luoboling Copper-Molybdenum mine now, but mine carried out the UCS laboratory test for some rock types in the engineering geological investigation phase. The mechanical properties of different rock types are listed in Table 1. As seen from Table 1, the mechanical properties of the same rock types also have a big difference. In this paper, the main purpose was to determine the relationship between cylinder and half-cylinder cores in PLT, and calculate $Is_{(50)}$ of the half-cylinder cores. And $Is_{(50)}$ was constantly being used as a determination of UCS; therefore, the UCS of rock was a mainly considered factor in PLT. At the same time, in order to reduce the complexity of the DEM micro-mechanical parameter calibration, we selected three kinds of rock as shown in Table 1 (number 2 porphyritic granodiorite, number 3 granodiorite, and number 10 granodiorite porphyry) as the calibration objects.

The DEM [28] of structures in rock or soil required calibration of the FJM parameters of materials using UCS tests

[2, 32–38]. To simulate rocks with different UCS and PLSI, the tensile strength and cohesion of the FJM parameters were varied, while other parameters were kept constant.

The properties of the rock samples, such as UCS, Young's elastic modulus, and Poisson's ratio, were obtained through UCS tests. Figure 4 shows the stress-strain curves with three parameters ($p1$, $p2$, and $p3$) during the UCS tests. Figure 5 shows the load curves with three parameters ($p1$, $p2$, and $p3$) during the PLT, and the diameter of the cylinder specimen is 50 mm. The parameters of FJM with the properties of the rock are calibrated using UCS tests and PLT and are listed in Table 2. The ratios between UCS and $Is_{(50)}$ were 21.76 ($p1$), 23.80 ($p2$), and 22.47 ($p3$), which confirmed the suggested values (the ratio between UCS and $Is_{(50)}$ varies between 20 and 25) given by ISRM (1985). Comparing Tables 1 and 2, the micromechanical parameters ($p1$, $p2$, and $p3$) in Table 2 correspond to the mechanical properties (number 2 porphyritic granodiorite, number 3 granodiorite, and number 10 granodiorite porphyry) in Table 1.

3.3. Microfractures under the PLT. The specimen was composed of bonded particles and failed under the point load. A combination of tensile and shear failure occurred in the selected bonded contacts and resulted in the failure of the specimen, and tension fractures or shear fractures were generated in the specimen. For example, the parameter of the numerical model was $p1$, and the distance D between two contact points was 30 mm. Figure 6 shows the fracture models of the half-cylinder (the length/diameter ratio is 2) and cylinder specimens (the length/diameter ratio is 1.2) under the point load.

As seen from Figure 6, the shear fractures generate around the two contact points at the beginning of loading. As loading increases, the tension fractures generate beyond a certain distance from the two contact points, and the number of tension fractures increases dramatically. The results are shown in Figure 6; the numbers of tension fractures and failure load of the half-cylinder specimens are higher than those of the cylinder specimen, but the number of shear fractures of the half-cylinder specimen is very close to that of the cylinder specimen. This was because the cross-sectional area of the half-cylinder specimen was larger than that of the cylinder specimen when they had the same D . To investigate the correlations of the failure load between cylinder and half-cylinder specimens, we carried out the PLT of the cylinder and half-cylinder specimens using the numerical model.

3.4. PLT of Cylinder Specimen. Diameters of boreholes were mainly 75 mm at the exploration stage of the Luoboling Copper-Molybdenum mine. Therefore, the diameters of the cylinder cores were from 50 mm to 70 mm. The cylinder cores were cut into two pieces (the half-cylinder cores) and so the radii of the half-cylinder core were 25–35 mm. And a large amount of the half-cylinder cores was 25–28 mm in radius that based on field measurement. According to the above analysis, the diameters of the cylinder specimens were determined. The diameters of the cylinder specimens were 18 mm, 22 mm, 26 mm, 30 mm, 34 mm, 38 mm, and 50 mm,

TABLE 1: The mechanical properties of different rock types.

Number	Rock type	Sample depth (m)	UCS (MPa)	Young's elastic modulus (GPa)	Poisson's ratio
1	Granodiorite	696.6–701.7	67.0	33.7	0.24
2	Porphyritic granodiorite	873.2–885.4	89.6	43.7	0.22
3	Granodiorite	423.7–430.5	55.7	42.9	0.21
4	Granodiorite	729.4–739.4	103.8	41.5	0.21
5	Porphyritic granodiorite	855.5–861.3	93.5	38.8	0.23
6	Granodiorite porphyry	851.0–863.0	99.6	40.7	0.21
7	Granodiorite	471.0–478.0	24.2	41.0	0.20
8	Granodiorite	477.8–483.0	43.4	61.0	0.25
9	Granodiorite porphyry	503.8–507.9	90.8	36.0	0.21
10	Granodiorite porphyry	531.5–534.8	28.4	44.8	0.21
11	Granodiorite porphyry	463.1–474.6	71.6	33.5	0.24

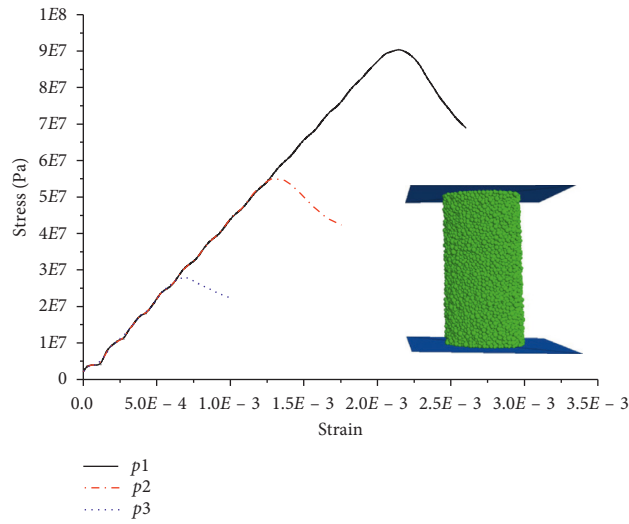


FIGURE 4: The stress-strain curves.

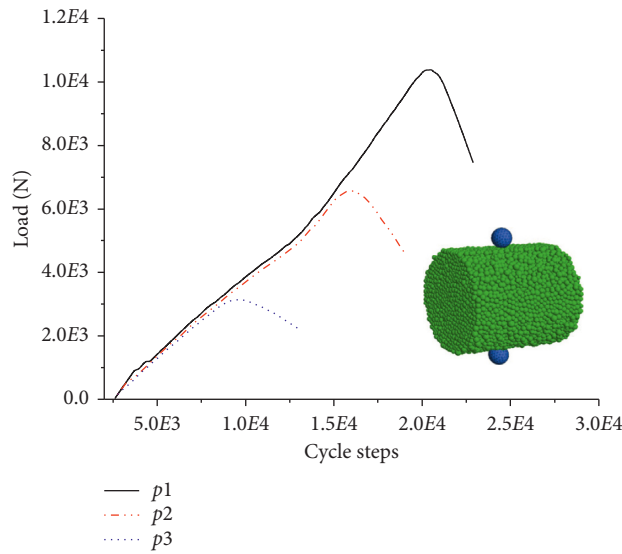


FIGURE 5: The point load test curves.

and the length/diameter ratios were 1.2, according to the suggestion of ISRM (1985). Figure 7 shows the failure load against different diameters on the cylinder specimens with

three parameters. According to Figure 7, the failure load increases with the increase in diameters of cylinder specimens. Then, we used formulae (1) and (2) to calculate $Is_{(50)}$,

TABLE 2: Parameters applied to the numerical model.

	Description	$p1$	$p2$	$p3$
Particle-based properties	Particle radius (mm)	2~3	2~3	2~3
	Particle density (g/cm^3)	2.70	2.70	2.70
FJM parameters	Effective modulus (GPa)	15.00	15.00	15.00
	Normal-to-shear stiffness ratio	0.36	0.36	0.36
	Friction angle ($^\circ$)	52.00	52.00	52.00
	Friction coefficient	0.50	0.50	0.50
	Tensile strength (MPa)	1.00	0.70	0.30
	Cohesion (MPa)	20.00	12.00	5.80
Properties	UCS (MPa)	90.54	55.70	28.31
	Young's elastic modulus (GPa)	43.87	43.28	44.30
	Poisson's ratio	0.21	0.21	0.20
	Failure load of PLT (kN)	10.40	6.59	3.14
	$Is_{(50)}$ (MPa)	4.16	2.64	1.26

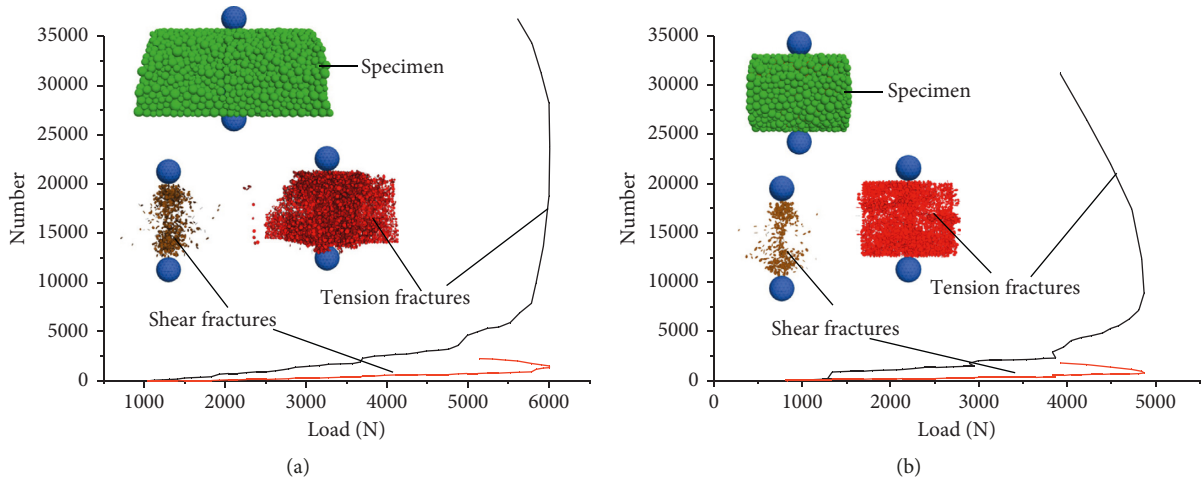


FIGURE 6: The fracture models of (a) half-cylinder specimens and (b) cylinder specimens.

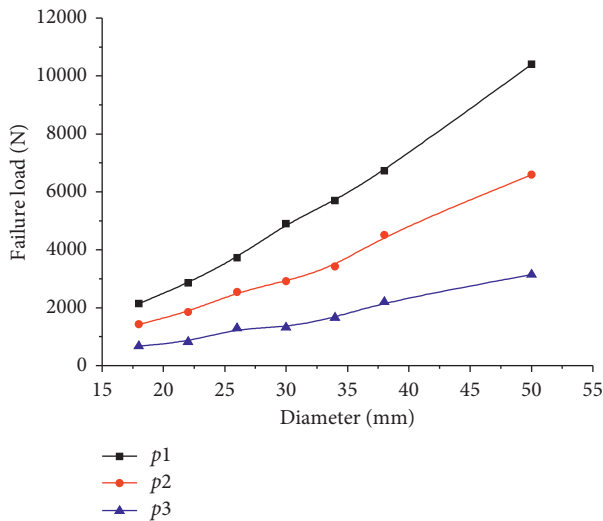


FIGURE 7: Results of the failure load with various diameters on the cylinder specimens.

and the results are listed in Table 3. As seen from Table 3, the results of $Is_{(50)}$ corresponding to different diameters were very close under the same parameters, and the CV of the

TABLE 3: $Is_{(50)}$ of the cylinder specimens.

Diameter (mm)	$p1$ $Is_{(50)}$ (MPa)	$p2$ $Is_{(50)}$ (MPa)	$p3$ $Is_{(50)}$ (MPa)
18	4.16	2.78	1.32
22	4.06	2.64	1.18
26	4.10	2.80	1.43
30	4.32	2.57	1.16
34	4.14	2.49	1.20
38	4.11	2.76	1.34
50	4.16	2.63	1.26
Mean	4.15	2.67	1.27
Standard deviation	0.08	0.11	0.09
CV	0.02	0.04	0.07

results were 0.02 ($p1$), 0.04 ($p2$), and 0.07 ($p3$). These results also show that the numerical model of PLT was feasible.

3.5. PLT of Half-Cylinder Specimens. $Is_{(50)}$ was affected by different failure loads, rock sizes, rock shapes, and loading modes. For the PLT of the half-cylinder specimens, the loading direction of PLT was only along the radial direction, and the length/diameter ratio and the distance D between two contact points were calculated. D was the radius of the

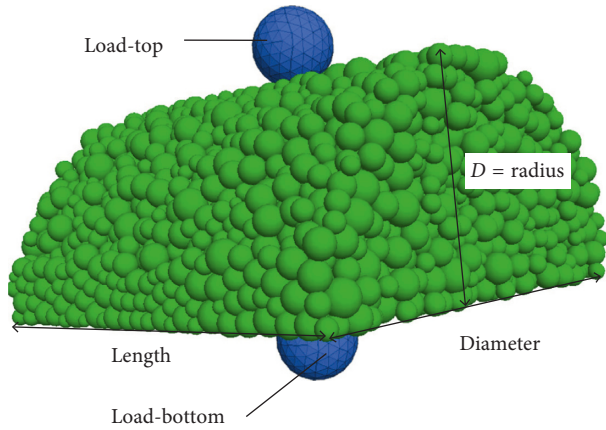


FIGURE 8: The numerical model of half-cylinder specimens.

half-cylinder specimens. Figure 8 shows the sizes and numerical model of the half-cylinder.

3.5.1. Influence of the Length/Diameter Ratio for Failure Load. To obtain the stable value of the failure load for the half-cylinder specimens, the numerical PLT of the half-cylinder specimen was conducted. Figure 9 shows the results of the failure load with the length/diameter ratio under the three parameters of the numerical model, when the radii of the half-cylinder specimens were 22 mm, 26 mm, and 30 mm. According to Figure 9, the failure load increases first and then tends to stabilize with the increase in the length/diameter ratio. The values of the failure load become stable when the length/diameter ratio was higher than 0.9.

3.5.2. Influence of the Distance D between Two Contact Points for Failure Load. To determine the influence of the distance D between two contact points (the radius of the half-cylinder specimen) for the failure load, the numerical PLT of the half-cylinder specimen was conducted. Figure 10 shows the curves of the distance D with the failure load under the three parameters, when the radii of the half-cylinder specimens are 18 mm, 22 mm, 26 mm, 30 mm, 34 mm, 38 mm, and 50 mm and the length/diameter ratios are 1. According to Figure 10, the failure load increases with the increase of the distance D .

4. Laboratory Tests

To verify the accuracy and reliability of the numerical model, laboratory tests were carried out on granitic rock and sandstone. The selected granitic rock and sandstone had the same lithology and no obvious discontinuities. According to the results of the numerical model, the size parameters of the specimens were determined and are listed in Table 4. According to Table 4, the specimens of the cylinder and half-cylinder were taken, and the number of tests per specimen was fixed at 10. Figure 11 shows the specimens of granitic rock and sandstone after failure and the PLT of the laboratory tests.

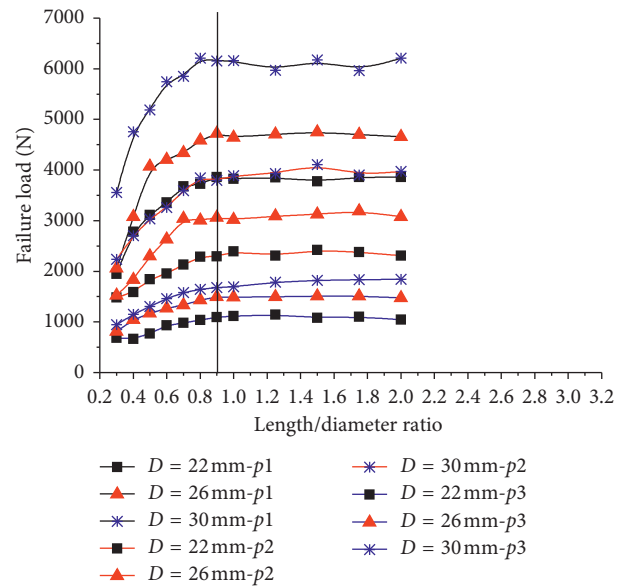


FIGURE 9: The results of the failure load with the length/diameter ratio.

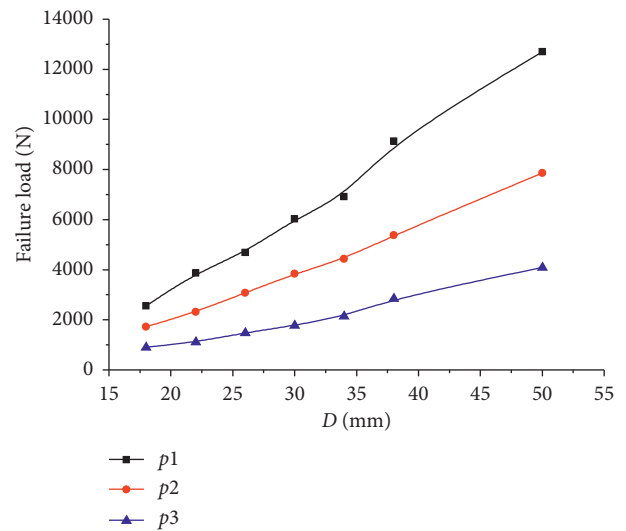


FIGURE 10: Results of the failure load with the distance D .

TABLE 4: Size parameters of the laboratory tests.

Specimen	D (mm)	Length (mm)	Length/diameter ratio
Cylinder	50	60	1.200
	40	50	1.250
	25	30	1.200
Half-cylinder	50	110	1.100
	40	90	1.125
	25	70	1.400
	25	55	1.100
	25	45	0.900
	25	35	0.700
	25	25	0.500

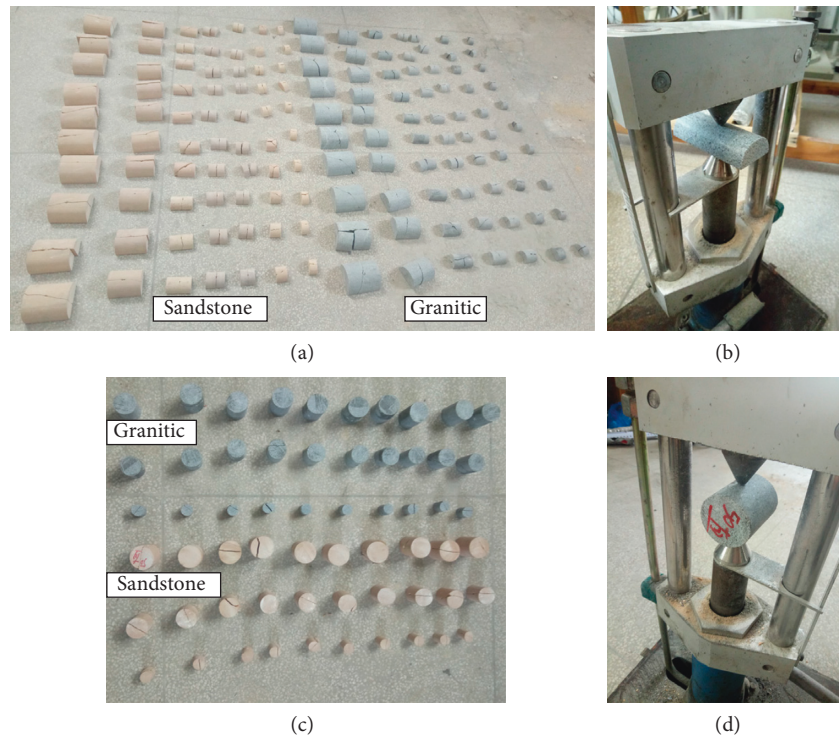


FIGURE 11: Laboratory point load tests: (a) the half-cylinder specimens, (b) PLT of the half-cylinder specimens, (c) the cylinder specimens, and (d) PLT of the cylinder specimens.

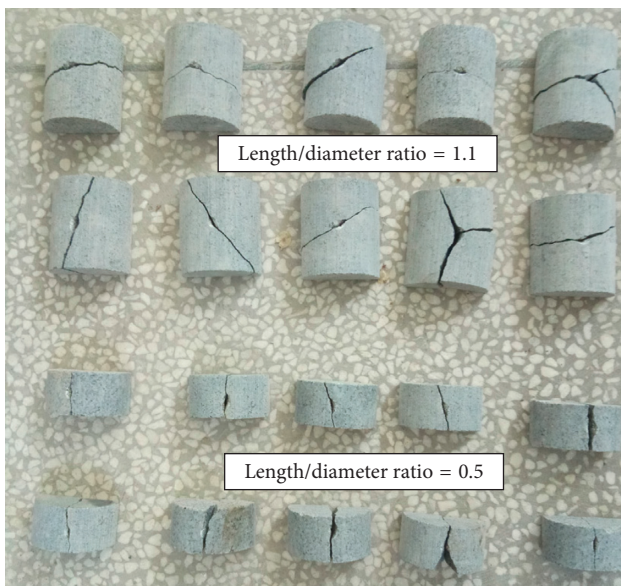


FIGURE 12: The failure surface of the half-cylinder specimens.

The directions of failure surface of the half-cylinder specimens were along the axial direction (as shown in Figure 12, where the length/diameter ratio is 0.5), when the length/diameter ratio was relatively small. With the increase of the length/diameter ratio, the directions of failure surface were along different directions (as shown in Figure 12 where the length/diameter ratio is 1.1). Thus, it can be seen that the length played a major role in the failure load when the length/diameter ratio was relatively small.

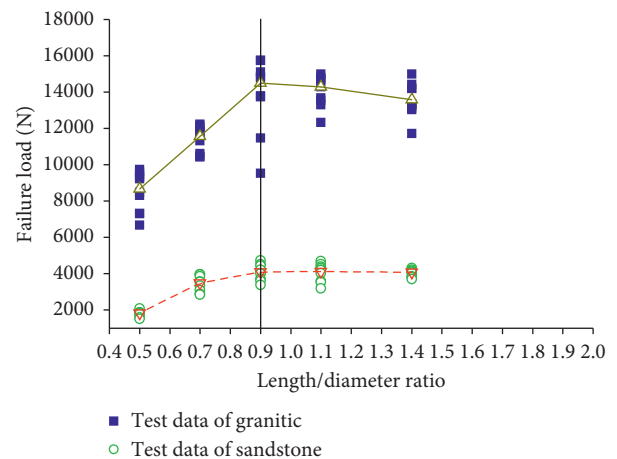


FIGURE 13: The results of the failure load with the length/diameter ratio from the laboratory tests.

We processed the test according to the calculation procedures of ISRM. Figure 13 shows the test results of the length/diameter ratio with the failure load. Figure 14 shows the test results of the distance D with the failure load.

As seen from Figure 13, the calculation values of the failure load become stable when the length/diameter ratio is higher than 0.9. According to the results of Figure 14, the failure load increases with the increase of the distance D , and the failure loads of the half-cylinder specimens are larger than the cylinder specimens under the same D and lithology conditions.

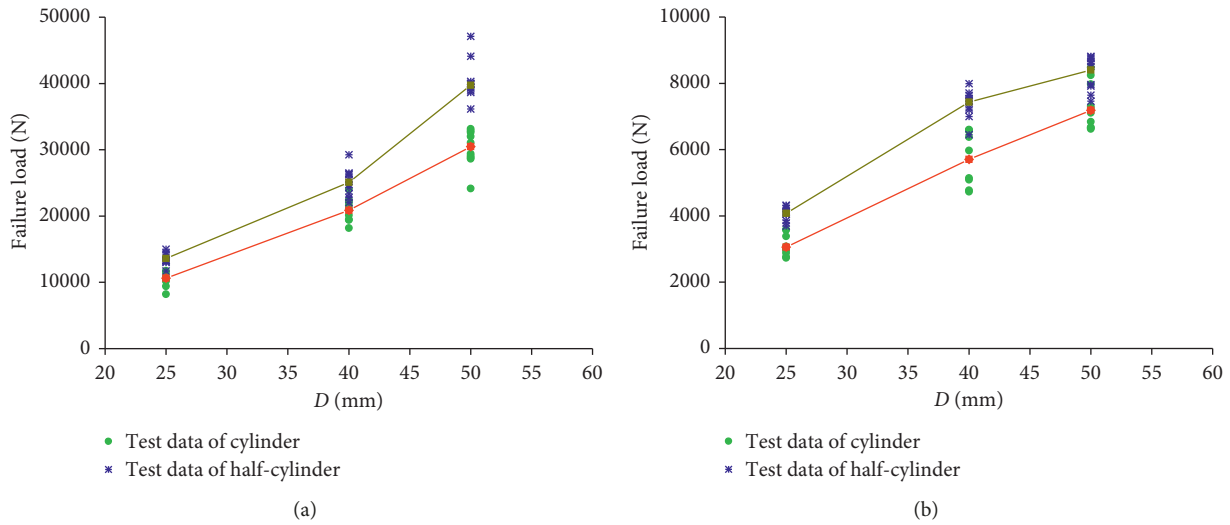


FIGURE 14: The results of the failure load with the distance D from the laboratory tests: (a) granitic and (b) sandstone.

5. Conclusions and Discussion

In this study, the PLT of half-cylinder specimens was investigated. For this purpose, the numerical model and laboratory tests were conducted on the cylinder and half-cylinder specimens. We determined the size (the length/diameter ratio) of the half-cylinder specimens and the correlation between cylinder and half-cylinder specimens. According to Figures 9 and 13, the value of the length/diameter ratio needs to be higher than 0.9 in the PLT of the half-cylinder specimens. The failure load ratios between cylinder and half-cylinder specimens are presented in Figure 15, with the same distance D and lithology conditions. The average of ratios is 0.793 (approximately 0.8), and the CV is 0.048. The results show that $Is_{(50)}$ of the half-cylinder cores could be calculated by formulae (1) and (2), and it was necessary to satisfy the conditions that the length/diameter ratio be higher than 0.9 and the failure load value be multiplied by 0.8. According to the above conclusions, $Is_{(50)}$ of half-cylinder cores in Figure 2 is recalculated, and we remove two test values that the length/diameter ratio of specimens is less than 0.9. The calculation result of $Is_{(50)}$ is 3.698 MPa, and the CV is 0.187. In conclusion, we determined $Is_{(50)}$ by PLT of the half-cylinder cores.

The advantage of PLT for half-cylinder cores is that we combined $Is_{(50)}$ with ore body information. The ore body was achieved by the chemical analysis of drilling cores, and we selected some drilling cores that intersected with the ore body. We carried out the PLT for these drilling cores. According to the ISRM suggestions and the findings of the half-cylinder cores, the values of $Is_{(50)}$ were calculated. Based on $Is_{(50)}$ and the position coordinates of the cores, we built the spatial distribution maps (Figure 16) using the method of inverse distance weight. Figure 16 can be used as an index for the classification of the rock mass strength and a reference for mining engineering design.

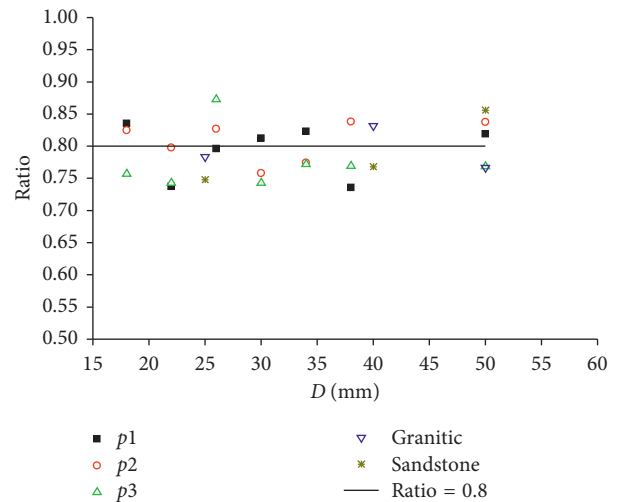


FIGURE 15: Ratio of the failure load against distance D with various forms of numerical models and laboratory tests.

Data from the numerical model or laboratory tests exhibit some scatter. The scatter of data is due to the algorithm of DEM in the numerical model. In the dynamic simulation of DEM, the selected timestep is very small, and the velocity and acceleration of the particles are constant in a timestep. The movement of particles only affects the particles that are directly contacted. The contact forces acting on the particle or wall are determined by the directly contacted particles. In the numerical model of PLT, the load of the specimen is imposed by giving the two load points a constant velocity. The value of the load is calculated from the mean of the two load points in a timestep. However, the particles that are in contact with the two load points are different in a certain timestep during the point loads (the concentrated loads). In other words, the contact states between particles and load points are different. Accordingly, the contact forces at the two points are different (as shown in Figure 17). However, the difference

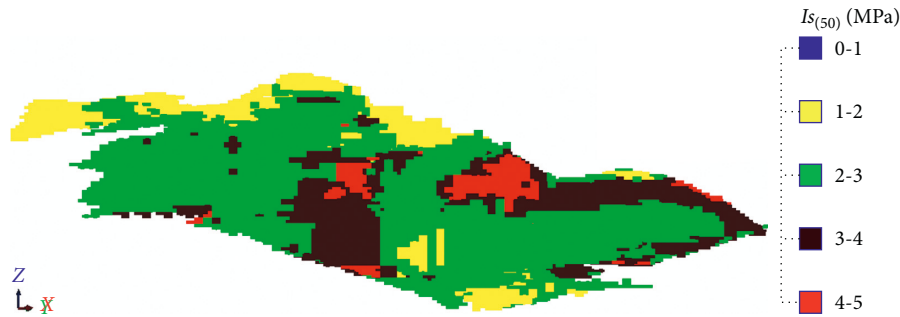


FIGURE 16: The spatial distribution map of $I_{s(50)}$.

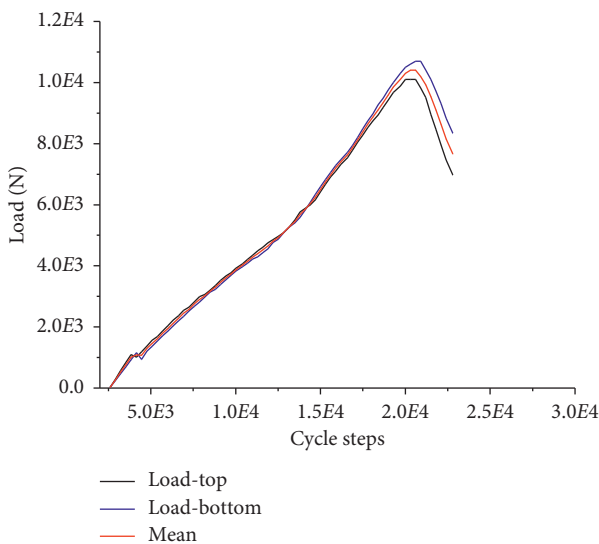


FIGURE 17: The contact forces at the two points of the numerical model.

between the two contact points is relatively small at the same timestep. The results of the numerical model are still credible. The results of laboratory tests also exhibit some scatter, which is believed to have occurred because of the cracks or anisotropic nature of specimens. The cracks may be naturally present in the rock and may also occur during sample preparation. To decrease the scatter, the number of specimens was fixed at 10 in this test. However, the scatter of test results is still lower than that of other test results, especially during the field testing.

In this study, cracks and joints in specimens are not considered either in the numerical models or in the laboratory tests. The cracks and joints in specimens will affect the failure load and the failure surface under the point load, which should be examined in future studies.

Data Availability

The data used to support the findings of this study are available from the corresponding author upon request.

Conflicts of Interest

The authors declare that they have no conflicts of interest.

Acknowledgments

The study was jointly supported by grants from the Key Program of National Natural Science Foundation of China (Grant no. 51534003) and the National Key Research and Development Program of China (Grant no. 2016YFC0801601). The authors are grateful for their support.

References

- [1] R. H. C. Wong, K. T. Chau, J.-H. Yin, D. T. W. Lai, and G.-S. Zhao, "Uniaxial compressive strength and point load index of volcanic irregular lumps," *International Journal of Rock Mechanics and Mining Sciences*, vol. 93, pp. 307–315, 2017.
- [2] H. Ozturk and M. Altinpinar, "The estimation of uniaxial compressive strength conversion factor of trona and interbeds from point load tests and numerical modeling," *Journal of African Earth Sciences*, vol. 131, pp. 71–79, 2017.
- [3] J. A. Franklin, "Suggested method for determining point load strength," *International Journal of Rock Mechanics and Mining Sciences & Geomechanics Abstracts*, vol. 22, no. 2, pp. 51–60, 1985.
- [4] E. Broch and J. Franklin, "The point-load strength test," *International Journal of Rock Mechanics and Mining Sciences & Geomechanics Abstracts*, vol. 9, no. 6, pp. 669–676, 1972.
- [5] N. Barton, "Some new Q-value correlations to assist in site characterisation and tunnel design," *International Journal of Rock Mechanics and Mining Sciences*, vol. 39, no. 2, pp. 185–216, 2002.
- [6] C. O. Aksoy, "Review of rock mass rating classification: historical developments, applications, and restrictions," *Journal of Mining Science*, vol. 44, no. 1, pp. 51–63, 2008.
- [7] K. Karaman, A. Kaya, and A. Kesimal, "Use of the point load index in estimation of the strength rating for the RMR system," *Journal of African Earth Sciences*, vol. 106, pp. 40–49, 2015.
- [8] R. A. Bearman, "The use of the point load test for the rapid estimation of Mode I fracture toughness," *International Journal of Rock Mechanics and Mining Sciences*, vol. 36, no. 2, pp. 257–263, 1999.
- [9] T. N. Singh, A. Kainthola, and A. Venkatesh, "Correlation between point load index and uniaxial compressive strength for different rock types," *Rock Mechanics and Rock Engineering*, vol. 45, no. 2, pp. 259–264, 2011.
- [10] M. Kohno and H. Maeda, "Relationship between point load strength index and uniaxial compressive strength of hydrothermally altered soft rocks," *International Journal of Rock Mechanics and Mining Sciences*, vol. 50, pp. 147–157, 2012.

- [11] D. A. Mishra and A. Basu, "Use of the block punch test to predict the compressive and tensile strengths of rocks," *International Journal of Rock Mechanics and Mining Sciences*, vol. 51, pp. 119–127, 2012.
- [12] S. Kahraman, "The determination of uniaxial compressive strength from point load strength for pyroclastic rocks," *Engineering Geology*, vol. 170, pp. 33–42, 2014.
- [13] A. F. Elhakim, "The use of point load test for Dubai weak calcareous sandstones," *Journal of Rock Mechanics and Geotechnical Engineering*, vol. 7, no. 4, pp. 452–457, 2015.
- [14] J.-H. Yin, R. H. C. Wong, K. T. Chau, D. T. W. Lai, and G.-S. Zhao, "Point load strength index of granitic irregular lumps: size correction and correlation with uniaxial compressive strength," *Tunnelling and Underground Space Technology*, vol. 70, pp. 388–399, 2017.
- [15] M. Greminger, "Experimental studies of the influence of rock anisotropy on size and shape effects in point-load testing," *International Journal of Rock Mechanics and Mining Sciences & Geomechanics Abstracts*, vol. 19, no. 5, pp. 241–246, 1982.
- [16] E. Broch, "Estimation of strength anisotropy using the point-load test," *International Journal of Rock Mechanics and Mining Sciences & Geomechanics Abstracts*, vol. 20, no. 4, pp. 181–187, 1983.
- [17] G.-R. Khanlari, M. Heidari, A.-A. Sepahigero, and D. Fereidooni, "Quantification of strength anisotropy of metamorphic rocks of the Hamedan province, Iran, as determined from cylindrical punch, point load and Brazilian tests," *Engineering Geology*, vol. 169, pp. 80–90, 2014.
- [18] K. T. Chau and X. X. Wei, "Spherically isotropic, elastic spheres subject to diametral point load strength test," *International Journal of Solids and Structures*, vol. 36, no. 29, pp. 4473–4496, 1999.
- [19] A. R. Russell and D. M. Wood, "Point load tests and strength measurements for brittle spheres," *International Journal of Rock Mechanics and Mining Sciences*, vol. 46, no. 2, pp. 272–280, 2009.
- [20] D. W. Hobbs, "A simple method for assessing the uniaxial compressive strength of rock," *International Journal of Rock Mechanics and Mining Sciences & Geomechanics Abstracts*, vol. 1, no. 1, pp. 5–15, 1964.
- [21] Y. Hiramatsu and Y. Oka, "Determination of the tensile strength of rock by a compression test of an irregular test piece," *International Journal of Rock Mechanics and Mining Sciences & Geomechanics Abstracts*, vol. 3, no. 2, pp. 89–90, 1966.
- [22] L. A. Panek and T. A. Fannon, "Size and shape effects in point load tests of irregular rock fragments," *Rock Mechanics and Rock Engineering*, vol. 25, no. 2, pp. 109–140, 1992.
- [23] K. T. Chau and R. H. C. Wong, "Uniaxial compressive strength and point load strength of rocks," *International Journal of Rock Mechanics & Mining Sciences and Geomechanics Abstracts*, vol. 33, no. 2, pp. 183–188, 1996.
- [24] V. Palchik and Y. H. Hatzor, "The influence of porosity on tensile and compressive strength of porous chalks," *Rock Mechanics and Rock Engineering*, vol. 37, no. 4, pp. 331–341, 2004.
- [25] G. Tsiambaos and N. Sabatakakis, "Considerations on strength of intact sedimentary rocks," *Engineering Geology*, vol. 72, no. 3–4, pp. 261–273, 2004.
- [26] M. Fener, S. Kahraman, A. Bilgil, and O. Gunaydin, "A comparative evaluation of indirect methods to estimate the compressive strength of rocks," *Rock Mechanics and Rock Engineering*, vol. 38, no. 4, pp. 329–343, 2005.
- [27] M. Fener and I. Ince, "Influence of orthoclase phenocrysts on point load strength of granitic rocks," *Engineering Geology*, vol. 141–142, pp. 24–32, 2012.
- [28] P. A. Cundall and O. D. L. Strack, "A discrete numerical model for granular assemblies," *Geotechnique*, vol. 29, no. 1, pp. 47–65, 1979.
- [29] Itasca Consulting Group, *PFC Version 5.0 User's Manual*, Itasca Consulting Group, Minneapolis, MN, USA, 2017.
- [30] S. Wu and X. Xu, "A study of three intrinsic problems of the classic discrete element method using flat-joint model," *Rock Mechanics and Rock Engineering*, vol. 49, no. 5, pp. 1813–1830, 2015.
- [31] K. Li, Y. Cheng, and X. Fan, "Roles of model size and particle size distribution on macro-mechanical properties of Lac du Bonnet granite using flat-joint model," *Computers and Geotechnics*, vol. 103, pp. 43–60, 2018.
- [32] N. Cho, C. D. Martin, and D. C. Segol, "A clumped particle model for rock," *International Journal of Rock Mechanics and Mining Sciences*, vol. 44, no. 7, pp. 997–1010, 2007.
- [33] J. Yoon, "Application of experimental design and optimization to PFC model calibration in uniaxial compression simulation," *International Journal of Rock Mechanics and Mining Sciences*, vol. 44, no. 6, pp. 871–889, 2007.
- [34] S.-Q. Yang, Y.-H. Huang, H.-W. Jing, and X.-R. Liu, "Discrete element modeling on fracture coalescence behavior of red sandstone containing two unparallel fissures under uniaxial compression," *Engineering Geology*, vol. 178, pp. 28–48, 2014.
- [35] X. Yang, H. Jing, and K. Chen, "Numerical simulations of failure behavior around a circular opening in a non-persistently jointed rock mass under biaxial compression," *International Journal of Mining Science and Technology*, vol. 26, no. 4, pp. 729–738, 2016.
- [36] Y. L. Gui, Z. Y. Zhao, C. Zhang, and S. Q. Ma, "Numerical investigation of the opening effect on the mechanical behaviours in rocks under uniaxial loading using hybrid continuum-discrete element method," *Computers and Geotechnics*, vol. 90, pp. 55–72, 2017.
- [37] H. Wu, J. Kemeny, and S. Wu, "Experimental and numerical investigation of the punch-through shear test for mode II fracture toughness determination in rock," *Engineering Fracture Mechanics*, vol. 184, pp. 59–74, 2017.
- [38] D. Yin, S. Chen, X. Liu, and H. Ma, "Simulation study on strength and failure characteristics for granite with a set of cross-joints of different lengths," *Advances in Civil Engineering*, vol. 2018, Article ID 2384579, 10 pages, 2018.



Hindawi

Submit your manuscripts at
www.hindawi.com

